International Journal of Nanomedicine

Dovepress

open access to scientific and medical research

Open Access Full Text Article

ORIGINAL RESEARCH

Effective Combination of Isoniazid and Core-Shell Magnetic Nanoradiotherapy Against Gastrointestinal Tumor Cell Types

Hao Chen[1,*], Daoming Zhu[1,*], Liang Guo[2], Guoxin Li[1]

[1]Department of General Surgery & Guangdong Provincial Key Laboratory of Precision Medicine for Gastrointestinal Tumor, Nanfang Hospital, The First School of Clinical Medicine, Southern Medical University, Guangzhou, Guangdong, 510515, People's Republic of China; [2]Department of Plastic Surgery, Zhongnan Hospital of Wuhan University, Wuhan, 430071, People's Republic of China

*These authors contributed equally to this work

Correspondence: Guoxin Li; Liang Guo, Email gzliguoxin@163.com; guoliangwhzn@163.com

Introduction: Radiotherapy is a conventional treatment for gastrointestinal tumors. However, its therapeutic effect might not be satisfactory because of factors such as radio-resistance of tumor cells and dose reduction applied to avoid damage to normal tissues. We developed a novel combination therapy involving the use of isoniazid (INH) and core-shell magnetic nanospheres (NPs) to enhance the efficacy of radiotherapy.

Methods: Magnetic core-shell NPs were synthesized. The shell manganese dioxide (MnO_2) reacted with intracellular glutathione to produce Mn^{2+}, which decomposed hydrogen peroxide (H_2O_2) to hydroxyl radicals (·OH) in the presence of INH to produce sufficient amount of reactive oxygen species. In addition to this chemodynamic therapy, MnO_2 catalyzed H_2O_2 to O_2, which alleviated hypoxia in tumors and thus enhanced the effect of radiotherapy. In addition, iron oxide (Fe_3O_4) and reduced Mn^{2+} were potential candidates for T_1–T_2 dual-mode magnetic resonance imaging (MRI) with remarkable magnetic targeting ability.

Results: NPs exhibited efficient tumor targeting performance under the magnetic field and improved T_1/T_2 dual-mode MRI, which elevated oxygen levels without toxicity to the mice to achieve remarkable therapeutic outcomes, reaching a tumor inhibition rate of 93.2%. Moreover, chemodynamic therapy mediated by INH and NPs enhanced the therapeutic effect of radiotherapy both in vivo and in vitro.

Conclusion: The results demonstrated that the combination of INH and NPs could be a novel strategy for radiosensitization with clinical potential.

Keywords: chemodynamic therapy, Fenton-like, isoniazid, radiotherapy, magnetic resonance imaging

Introduction

Radiotherapy (RT), an effective treatment for solid tumors, is applied in more than half of clinical cancer cases.[1–3] X-ray from RT can directly ionize the DNA molecules inside tumor cells,[4] and the reaction of DNA with oxygen causes DNA double-strand breaks.[5] Similarly, X-ray indirectly deposits energy inside tumor cells, and the hydrated electrons produced by ionized water molecules react with oxygen to form reactive oxygen species (ROS), which react with biological macromolecules, leading to cell apoptosis.[6,7] Thus, oxygen is a key factor in the course of RT. However, the inherent hypoxia of the tumor microenvironment (TME) significantly inhibits the effect of RT, leading to RT resistance.[8–10] In addition, glutathione (GSH) in the TME can eliminate free radicals, such as hydroxyl radicals (·OH), produced by RT and repair the DNA double-strand breaks caused by RT, thus adversely affecting the treatment.[11] Therefore, methods to improve the sensitivity of RT are necessary.

Compared to traditional chemotherapeutic drugs, nanomaterials can reduce the reaction with the physiological environment and prolong circulation time in vivo, thus aiding in tumor treatment.[7,12–15] Since the photoelectric effect

Received: 29 September 2021
Accepted: 16 January 2022
Published: 10 March 2022

beneficial to RT is proportional to $(Z/E)^3$ of the material, nanomaterials with a high atomic number can have a significant sensitization effect on RT.[16] Jia et al designed Au_8NCs with a precise atomic structure to sensitize highly effective RT by producing high amounts of ROS at a relatively low and safe radiation dose.[17,18] In addition, some nanomaterials can improve the TME (such as hypoxia, GSH, hydrogen peroxide [H_2O_2]) to decrease RT resistance.[19] Accordingly, Zhu et al designed a tumor cell membrane-coated manganese dioxide (MnO_2) nanozyme biomimetic system, which could react with tumors endogenously to produce abundant oxygen and enhance the effect of RT.[20] However, studies on RT sensitization by increasing oxygen levels are limited by the difficulty in oxygen delivery and limited oxygen carrying content, which diminish the sensitization effect.[21–23] Thus, the combination of RT and chemodynamic therapy, which does not require oxygen but can react with excess H_2O_2 in TME to produce ·OH for synergistic therapy, is a promising treatment approach.[24–30]

RT induces cell apoptosis through direct or indirect damage. Indirect damage is caused by ionizing radiation, producing ROS intracellularly. However, tumor cells might eliminate ROS. To improve the effect of RT, both the ROS amount produced and ROS protection should be considered. Isoniazid (INH), a clinical anti-tuberculosis drug, can interact with Mn^{2+} to produce highly toxic ·OH, which affects cancer treatment.[31] Cheng et al developed INH-supported WSSe/MnO_2 nanocomposites with mitochondrial targeting, which could induce ·OH generation via INH-induced tumor ablation in combination with photothermal therapy.[32] Based on Cheng et al's findings and accounting for the dependance of the degree of RT sensitization on the sensitivity of tumor cells to radiation and the amount of ROS in tumor cells, we designed Fe_3O_4@MnO_2 nanospheres (NPs) in combination with INH to achieve a synergy between RT and chemodynamic therapy (Scheme 1). A magnetic field (MF) was used to guide the enrichment of Fe_3O_4@MnO_2 nanoparticles at the tumor site. Under the acidic TME, the MnO_2 shell layer on the surface can consume GSH, which prevents removal of the ROS produced by RT and destroys the redox tumor environment, and can react with INH to generate highly toxic ·OH, which improves the curative effect of RT. In addition, owing to the presence of Mn^{2+}, Fe_3O_4@MnO_2 can be used as a contrast agent for enhanced T_1-weighted magnetic resonance imaging (MRI).[33] After the consumption of MnO_2, the exposed core

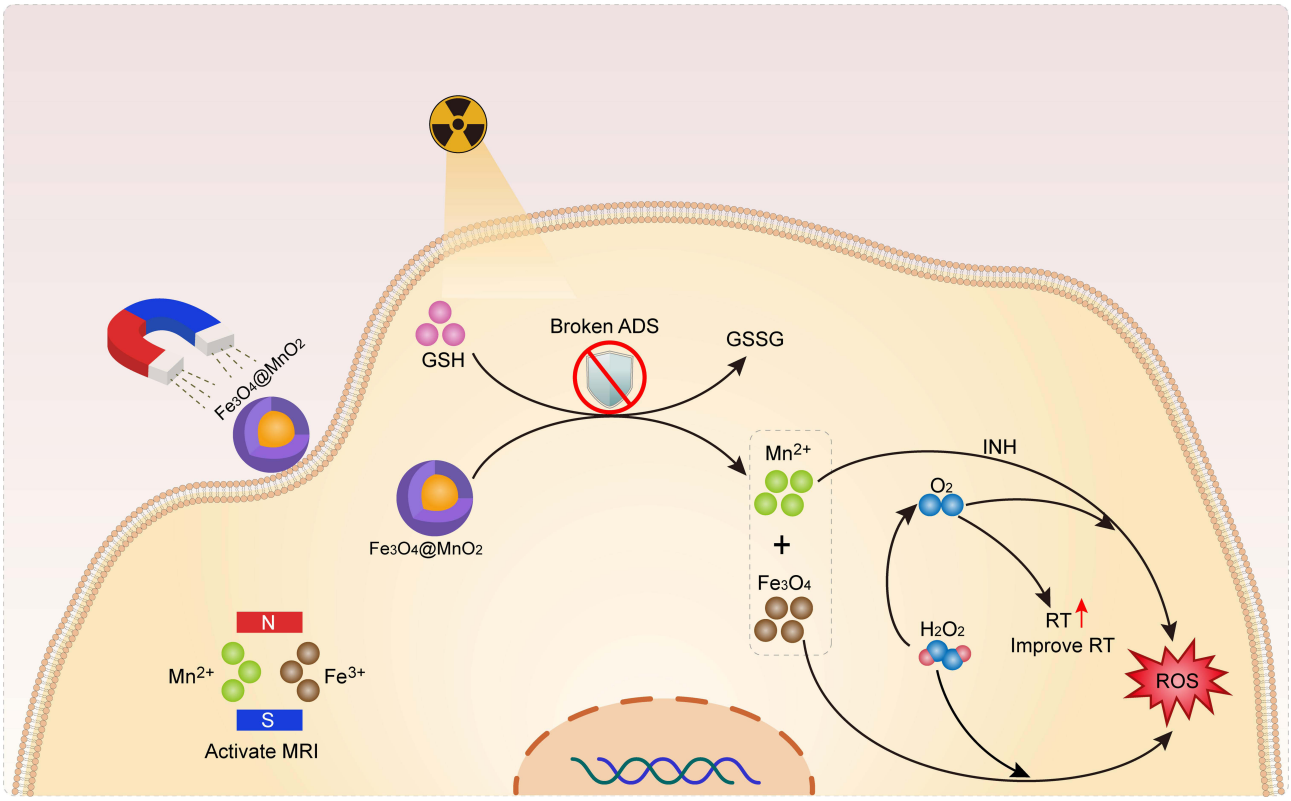

Scheme 1 Strategy of combination therapy via isoniazid and core-shell magnetic nanosphere to enhance radiotherapy.

Fe_3O_4 can react with endogenous H_2O_2 to generate ·OH, which can further kill tumor cells. Moreover, MnO_2 can decompose H_2O_2 to O_2 to alleviate hypoxia. Simultaneously, Fe_3O_4 can be used as a contrast agent for T_2-weighted MRI. Both Fe and Mn are essential trace elements in the human body, and INH is a medicine, thus ensuring the biocompatibility of the combined system of Fe_3O_4@MnO_2 and INH. Therefore, Fe_3O_4@MnO_2, as a contrast agent significantly improves the ability of T_1- and T_2-weighted MRI, and its combination with INH destroys the redox tumor environment and increases the ROS level in tumors to maximize the damage to cancer cells by ROS.

Materials and Methods

Synthesis and Characterization of Fe_3O_4@MnO_2

Based on the successful synthesis of Fe_3O_4@MnO_2 nanoparticles (NPs) by our research group in previous articles,[34] we will briefly introduce it here. Synthesis of Fe_3O_4@MnO_2 is roughly divided into two steps.

Synthesis of Fe_3O_4 NPs

First came the synthesis of Fe_3O_4 by hydrothermal method. $FeCl_3·6H_2O$ (1.35g, 5mm) was dissolved in ethylene glycol (40mL), and NaAc (3.6g) was added while stirring (30 minutes) until a transparent solution was formed. It was sealed in a stainless-steel autoclave containing teflon (50 mL capacity), heated at 200°C for 7h, and washed respectively several times with ethanol and distilled water after cooling to room temperature.

Synthesis of Fe_3O_4@MnO_2 Nanoparticles

And then the synthesis of core-shell Fe_3O_4@MnO_2 nanoparticles through a homogeneous precipitation method. The Fe_3O_4 (0.5 g) nanoparticles were added to 5% PEG (100 mL) for 30 min by ultrasonic agitation to form magnetic fluid. $KMnO_4$ (0.1975 g) and $(CH_3COO)_2Mn·4H_2O$ (0.46 g) were also dissolved in 5% PEG (100 mL) at room temperature. Finally, the above two solutions were mixed and reacted at 60°C for 4 h, and the resulting solution was washed several times with anhydrous ethanol.

Physical Characterization of NPs

The morphology of NPs NPs was observed by transmission electron microscopy (TEM; Tecnai G2 F20 S-Twin, FEI, USA) at 100 keV acceleration voltage. The phase structures were acquired by means of X-ray diffraction (XRD; Bruker D8 Advance, Germany) with Cu Kα radiation (λ = 0.15406 nm). The surface chemical elements and elements orbits were analyzed by XPS (ESCA-Lab250XI, Thermo Fisher Ltd., USA). The zeta potential and zeta diameter of NPs before and after 6 Gy irradiation were was determined using dynamic light scattering (Nano-Zen 3600, Malvern Instruments, UK).

Cell Culture

AGS cells were purchased from the Chinese Academy of Sciences, Shanghai, China. AGS cells were cultured in RPMI-1640 (HyClone, USA) containing 10% fetal bovine serum. Cells were maintained in a humidified incubator at 37 °C in an atmosphere of 5% CO_2.

Animal Models

6-week-old female nude BALB/c mice (purchased from Vital River Company, Beijing, China) were subcutaneously injected with 100 μL AGS cell suspension (1×10^7 cells/mL) on the right hip to establish tumor model. All procedures have been approved by protocols of the Institutional Animal Care and Use Committee (IACUC) of the Animal Experiment Center of Wuhan University (Approve No. AF146). In additional, All the in vivo experiments on mice according to the guideline for ethical review of animal welfare (GB/T 35892-2018) and guideline for euthanasia (GB/T 39760-2021) approved by standards approved by China.

In vivo HE Staining Sections

5 tumor-bearing mice were euthanized and their tumors and main organs were sliced and embedded in paraffin. Next, these tissue sections was stained using hematoxylin solution for 3–5 min and next treated with hematoxylin differentiation solution following by Treat the section with Hematoxylin Scott Tap Bluing, rinse with tap water.

In vivo Antitumor Study

When the tumor size approached 200mm^3, 30 mice were randomly divided into 6 groups (n=5) to receive various treatments: (1) PBS; (2) RT (6 Gy); (3) NPs (100 μL, 100 μg/mL) under MF; (4) NPs (100 μg/mL) under MF + INH (20 μg/mL); (5) NPs (100 μg/mL) + INH (20 μg/mL) 6 h before RT (6 Gy); (6) NPs (100 μg/mL) under MF + INH (20 μg/mL) 6 h before RT (6 Gy). A square magnet of 5000 Gauss was used for providing external magnetic field. Tumor length and width were measured with calipers every 2 days to obtain changes in tumor volume and to record changes in body weight.

Results and Discussion

First, we synthesized core-shell Fe_3O_4@MnO_2 NPs. The NPs were uniform with an average diameter of 234 nm under transmission electron microscopy (Figure 1A). Fe_3O_4 was covered with small particles of MnO_2 (Figure S1). X-ray diffraction exhibited both Fe_3O_4 (PDF#89-4319) and MnO_2 (PDF#81-2261; Figure 1B). The X-ray photoelectron spectroscopy spectrum of NPs further confirmed Fe and Mn in NPs (Figure 1C). Figure 1D and E show high-resolution spectra of Mn 2p and Fe orbits, respectively. Mn 2p was located at 642 and 654 eV, consistent with the characteristic peaks of Mn^{4+}. The Fe spectrum indicated the valences of Fe^{3+} and Fe^{2+} in NPs. Moreover, the zeta potential and diameter of NPs demonstrated no difference before and after irradiation (Figure S2), reflecting remarkable radiation ionizing stability.

Next, we assessed the ability of NPs to deplete the GSH in cells. Figure 2A shows the results. The amount of GSH consumption increased with time, and the consumption reached over 80% of the total amount of GSH at 210 s, indicating remarkable GSH depletion ability of NPs in vitro. Methylene blue (MB) is a typical indicator of ·OH generation since this blue dye can be degraded by ·OH. INH can react with Mn^{2+} to produce ·OH; therefore, $MnCl_2$ was used as a source of Mn^{2+} to verify this process. Figure 2B shows the absorbance change at 665 nm under various treatments. INH+Mn^{2+} might have induced MB degradation, but no apparent change in the MB concentration was observed in the presence of INH or $MnCl_2$ alone. Moreover, MB degradation was impaired after adding 10 mM GSH, owing to the scavenging effect.[26] Considering that NPs can be reduced by intracellular GSH to obtain Mn^{2+}, the

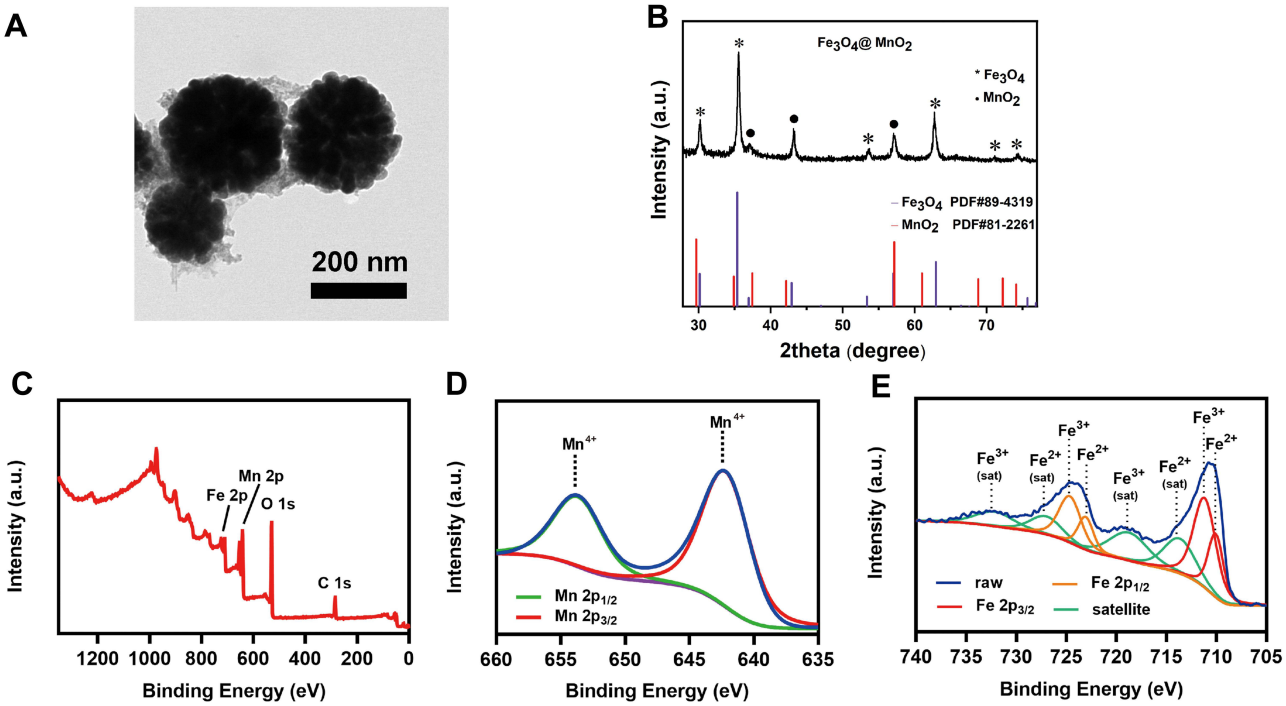

Figure 1 Structure and property characterizations. (**A**) TEM image, (**B**) XRD analysis. *Represents peaks of Fe_3O_4 and · represents peaks of MnO_2. (**C**) XPS spectra of Fe_3O_4@MnO_2 NPs. (**D**) Mn 2p and (**E**) Fe 2p of Fe_3O_4@MnO_2 NPs.

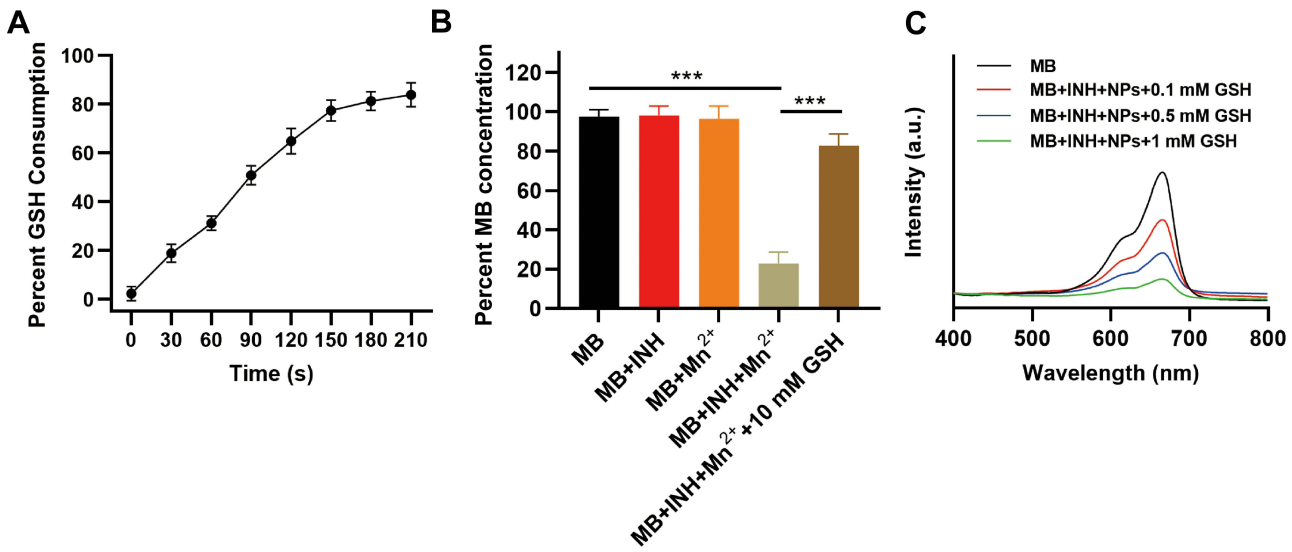

Figure 2 Fenton-like reaction assessment. (**A**) GSH consumption in existence with 100 μg/mL of NPs. (**B**) Percentage of MB concentration after various treatments. (**C**) MB degradation under various treatments. ***P < 0.005; Student's *t*-test.

reaction among INH, NPs, and GSH was investigated. Only in the presence of INH+NPs+GSH did the MB concentration decrease. However, the trend similarly decreased when the GSH concentration became 10 mM. Nevertheless, MB degradation caused by INH+Mn^{2+} reached 22.9%, which was 4.2 times greater than that caused by Mn^{2+}. Similarly, in a previous study, the intracellular concentration of GSH ranged from 0.1 to 10 mM when INH +NPs exhibited outstanding ·OH generation ability.[35] Figure 2C shows the ultraviolet–visible light absorption curves of MB under various treatments. Absorbance intensity decreased with MB+INH+NPs+0.1 Mm GSH compared to MB alone. In addition, the absorbance intensity decreased when the GSH concentration increased. INH, NPs, or INH+NPs exhibited no apparent degradation ability to MB.

Based on the mechanism effect, we evaluated the antitumor efficacy of this treatment strategy in vitro. Since biocompatibility should be assessed, cell viability was checked after incubation with NPs under concentrations ranging from 0 to 500 μg/mL (Figure S3). The cell viability was over 70% even at a concentration of 200 μg/mL. The hematolysis analysis also indicated satisfactory biocompatibility of NPs as a hematolysis rate lower than 3% at a concentration of 200 μg/mL (Figure S4).

RT induces cell apoptosis via DNA double-strand breaks. Therefore, it is compulsory to assess the extent of DNA double-strand breaks after various treatments. Cells pretreated with NPs+INH prior to RT exhibited remarkable DNA damage compared to RT alone (Figure 3A). Next, cell viability after various treatments were measured using Cell Counting Kit-8. Cells treated with NPs+INH exhibited suppression of cell viability owing to Fenton-like reactions (Figure 3B). However, the group treated with NPs+INH+RT showed a cell death rate of 38.9%, enhancing the effect of RT with the most effective cell killing ability. Moreover, 2', 7'-dichlorodihydrofluorescein was utilized to detect ROS (Figure 3C). The group treated with RT or NPs showed limited green fluorescence intensity compared to the group treated with NPs+INH. Among all the groups, cells treated with NPs+INH+RT generated the largest amount of ROS, consistent with the result of flow cytometry (Figure 3D). Colony formation assay, the gold standard method to evaluate radiosensitization, was conducted to assess the ability of this strategy to enhance the efficacy of RT. The curve represented the NPs+INH+RT group separate from the control group's curve with the most apparent distinction when irradiated with 6 and 8 Gy (Figure 3E). In addition, the sensitization enhancement ratio of the NPs+INH strategy was calculated to be 1.89. The wounding assay was conducted to infer the migration ability (Figure 3F). Subsequently, after 24 h, cells in the control group recovered rapidly. When the group treated with RT, NPs, and INH+NPs demonstrated limited cell migration ability, cells in groups treated with INH+NPs+RT exhibited most apparent inhibition of cell

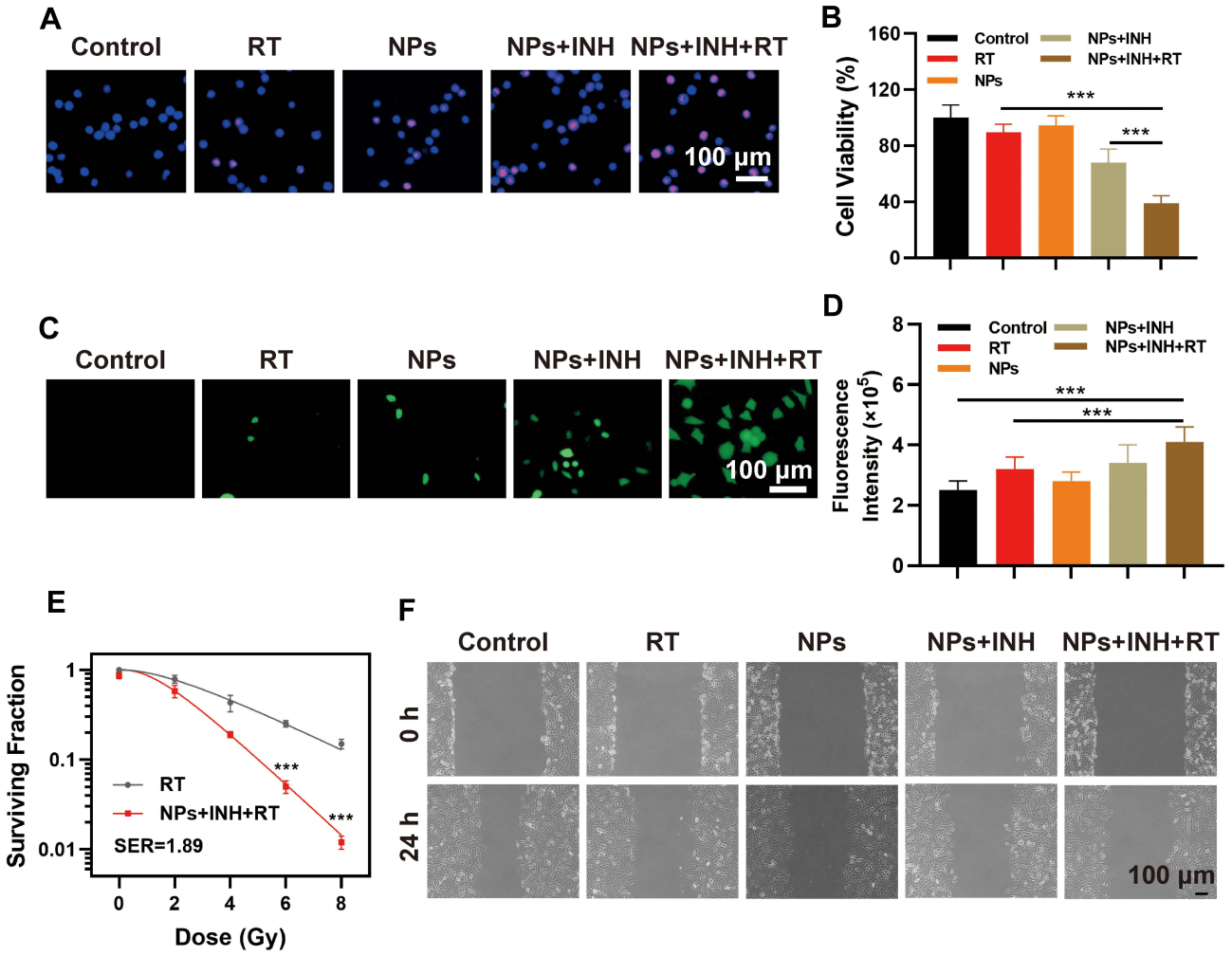

Figure 3 Antitumor efficacy in vitro. (**A**) γ-H_2AX staining of cells; (**B**) Cell viability tested using CCK 8 kit. (**C**) DCFH-DA staining of cells. (**D**) Fluorescence intensity detection using flow cytometry. (**E**) Colony formation assay. (**F**) Wounding assay. (RT: 6Gy; NPs: 100 μg/mL; INH: 20 μg/mL). ***P < 0.005; Student's *t*-test.

migration, leaving a huge gap between two cell communities. INH+NPs could dramatically enhance the efficacy of RT in vitro.

To further confirm the cell apoptosis induced by INH+NPs+RT, flow cytometry analysis was conducted. No cell apoptosis was observed in the control or NPs group (Figure S5), indicating no severe cytotoxicity of NPs to cells, whereas cell death occurred under the treatment of NPs+INH. Among all groups, cells treated with NPs+INH+RT showed most severe apoptosis (42.9%). Fe_3O_4, MnO_2, and INH induces cell apoptosis via the caspase mediated pathway, which involves caspase 3,[36] caspase 8,[37] and caspase 9.[38] Cell apoptosis in the NPs+INH+RT group was mediated by caspases 3, 8, and 9 through upregulated expression (Figure S6). Moreover, Z-VAD-FMK, a caspase inhibitor was also applied to confirm the apoptosis pathway (Figure S7). Cell viability exceeded 95% in the NPs+INH+RT group after adding Z-VAD-FMK and was 22.5% when treated with NPs+INH+RT alone, which indicated that cell apoptosis was suppressed by the caspase inhibitor.

Next, NPs were injected intravenously to evaluate the deposition ability of converting H_2O_2 to oxygen in vivo. Pimonidazole staining was used for hypoxia detection (Figure 4). The control group showed strong green fluorescence intensity, indicating severe hypoxia in the tumor region. After injecting NPs, the intensity of fluorescence decreased. Moreover, under the treatment of MF directing NPs, hypoxia in the tumor region was alleviated to a large extent. Moreover, the result of hypoxia-inducible factor 1-alpha staining confirmed that under MF, NPs could efficiently alleviate hypoxia at the tumor site (Figure S8). Thus, NPs under MF could reduce hypoxia in tumors.

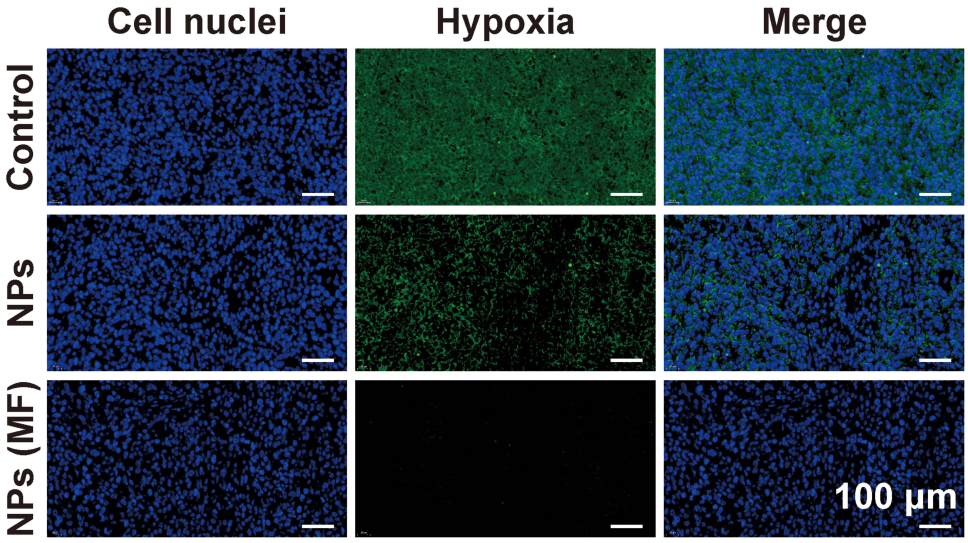

Figure 4 Pimonidazole staining of tumor slices 24 h post intravenous injection of PBS or NPs (100 μL, 100 μg/mL; Scale bar: 100 μm).

Further, we investigated the feasibility of this Fenton-like chemodynamic therapy strategy for radiosensitization on Aicardi-Goutières syndrome tumor-bearing mice. When the tumor volume reached approximately 200 mm^3, mice were subjected to the following treatment (five mice/group): (1) PBS; (2) RT (6 Gy); (3) NPs (100 μL, 100 μg/mL) under MF; (4) NPs (100 μg/mL) under MF + INH (20 μg/mL); (5) NPs (100 μg/mL) + INH (20 μg/mL) 6 h before RT (6 Gy); (6) NPs (100 μg/mL) under MF + INH (20 μg/mL) 6 h before RT (6 Gy). Subsequently, the body weight, tumor volume, and tumor weight were monitored (Figure S9, Figure 5A and B). The body weight did not change in any of the groups. The NPs+INH+RT treatment suppressed tumor growth apparently while the NPs+INH+RT(MF) group demonstrated most significant antitumor efficacy. The MF targeting ability was also confirmed. Mice receiving NPs (MF)+INH treatment exhibited slight tumor inhibition induced by chemodynamic therapy. Tumor growth was rapid in the RT and NPs treatment groups. Tumor weight showed significant tumor suppression in the NPs (MF)+INH+RT group compared to the NPs+INH(MF) or NPs+INH+RT group. Hematoxylin and eosin staining showed a slightly lower degree of cell apoptosis in NPs+INH(MF) and NPs+INH+RT groups than in the NPs+INH+RT(MF) group, whereas no tumor cell death occurred in the RT or NPs treatment group (Figure 5D). The architecture was significantly damaged in tumor slices treated with NPs+INH+RT(MF). To detect the amount of ROS produced, dihydroethidium was utilized for fluorescence staining of tumor slices. Consistent with the result in vitro, the group treated with NPs+INH(MF) showed an increased expression of ROS due to the chemodynamic therapy. NPs+INH+RT(MF) significantly elevated the ROS level in all groups. Moreover, hematoxylin and eosin staining of the main organs showed no lesions (Figure 5C), indicating good biocompatibility of the treatment strategy.

MRI was conducted to verify the T_1-/T_2-weighed contrast effect of NPs. NPs revealed a longitudinal relaxation rate of 5.44 in the presence of GSH (Figure S10). No accumulation in the tumor region was observed without MF. Conversely, the tumor region was brightened in the group guided by MF. The transverse relaxation rate of NPs was calculated to be 114.6. In accordance with the in vivo result of T_1 scanning, the tumor region was darker under MF. It can be concluded that NPs exhibit a superior tumor targeting ability under MF and can act as a contrast agent for T_1-/T_2-weighed MRI.

Conclusion

We introduced a novel strategy using chemodynamic therapy induced by INH and NPs to enhance RT, which demonstrated effective tumor suppression. In the presence of GSH, INH, and NPs, H_2O_2 converted to ·OH, which facilitated the chemodynamic therapy. Moreover, NPs under MF could target the tumor region. NPs catalyzed H_2O_2 to O_2, which alleviated hypoxia in tumors, and NPs exhibited significant T_1-/T_2- weighed imaging contrast ability both in vitro and

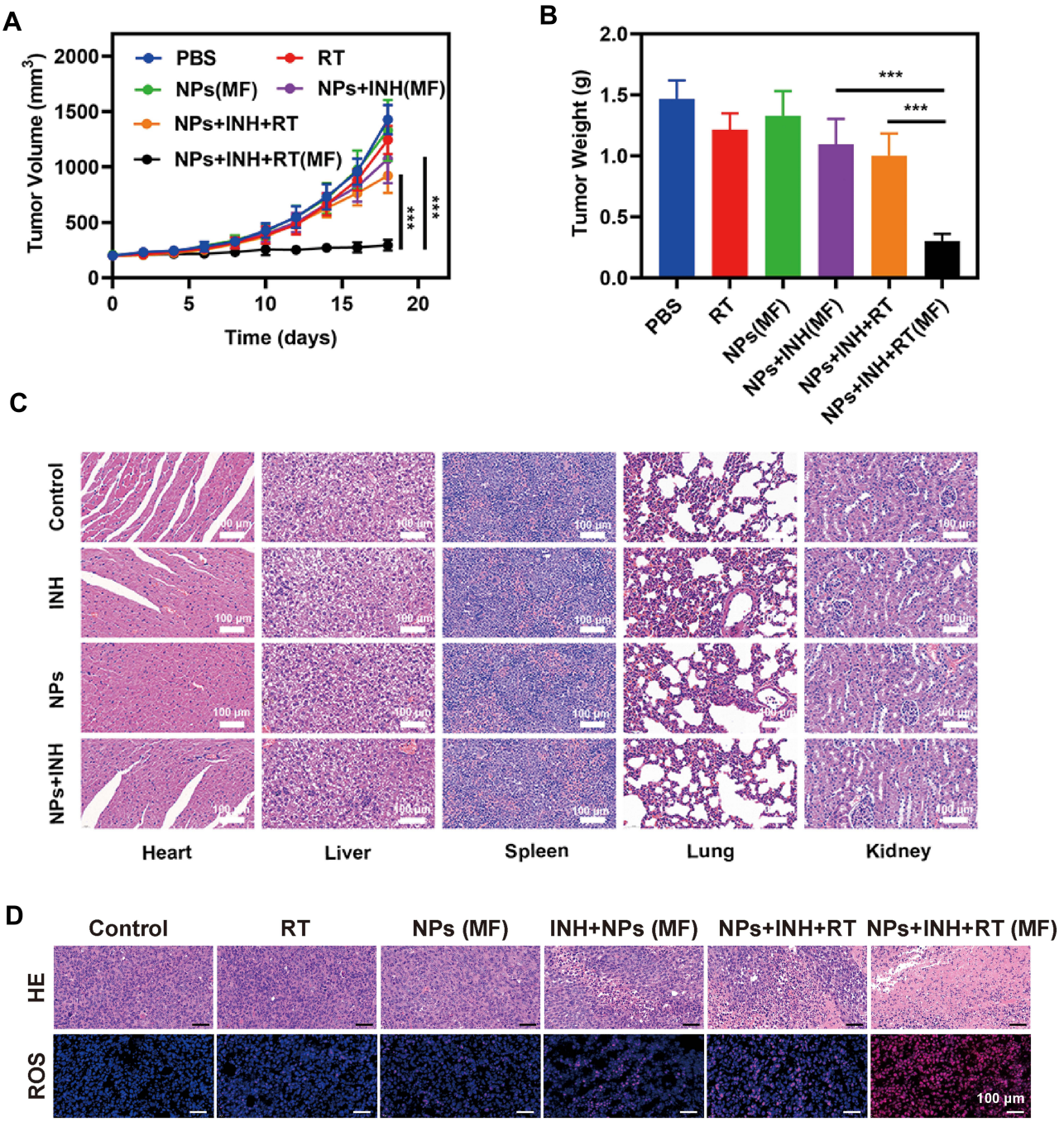

Figure 5 Antitumor efficacy in vivo. (**A**) Tumor volume changes and (**B**) tumor weights. (**C**) HE staining of main organs sections of mice (Scale bar: 100 μm) (**D**) HE staining and ROS staining of tumors of mice received different treatment (Scale bar: 100 μm). ***P < 0.005; Student's *t*-test.

in vivo. This therapeutic method of combining chemodynamic therapy with RT offers a novel strategy for tumor treatment.

Acknowledgment

This work was supported by grants from the Guangdong Provincial Key Laboratory of Precision Medicine for Gastrointestinal Cancer (2020B121201004), the Guangdong Provincial Major Talents Project (No.2019JC05Y361).

The authors would like to thank all the reviewers who participated in the review and MJEditor (www.mjeditor.com) for its linguistic assistance during the preparation of this manuscript.

Disclosure

The authors declare no competing interests in this work.

References

1. Verellen D, De Ridder M, Storme G. A short history of image-guided radiotherapy. *Radiother Oncol*. 2008;86(1):4–13. doi:10.1016/j.radonc.2007.11.023
2. Zheng N, Wang Q, Li C, et al. Responsive degradable theranostic agents enable controlled selenium delivery to enhance photothermal radiotherapy and reduce side effects. *Adv Healthc Mater*. 2021;10(10):e2002024. doi:10.1002/adhm.202002024
3. Sung H, Ferlay J, Siegel RL, et al. Global cancer statistics 2020: GLOBOCAN estimates of incidence and mortality worldwide for 36 cancers in 185 countries. *CA Cancer J Clin*. 2021;71(3):209–249. doi:10.3322/caac.21660
4. Cui FB, Li RT, Liu Q, et al. Enhancement of radiotherapy efficacy by docetaxel-loaded gelatinase-stimuli PEG-Pep-PCL nanoparticles in gastric cancer. *Cancer Lett*. 2014;346(1):53–62. doi:10.1016/j.canlet.2013.12.002
5. Lyu M, Zhu D, Duo Y, Li Y, Quan H. Bimetallic nanodots for tri-modal CT/MRI/PA imaging and hypoxia-resistant thermoradiotherapy in the NIR-II biological windows. *Biomaterials*. 2020;233:119656. doi:10.1016/j.biomaterials.2019.119656
6. Sun Q, Wu J, Jin L, et al. Cancer cell membrane-coated gold nanorods for photothermal therapy and radiotherapy on oral squamous cancer. *J Mater Chem B*. 2020;8(32):7253–7263. doi:10.1039/D0TB01063D
7. Liu T, Yang K, Liu Z. Recent advances in functional nanomaterials for X-ray triggered cancer therapy. *Prog Nat Sci*. 2020;30(5):567–576. doi:10.1016/j.pnsc.2020.09.009
8. Huang C, Wang FB, Liu L, et al. Hypoxic tumor radiosensitization using engineered probiotics. *Adv Healthc Mater*. 2021;10(10):e2002207. doi:10.1002/adhm.202002207
9. Wu S, Liu X, Ren J, Qu X. Glutathione depletion in a benign manner by MoS2 -based nanoflowers for enhanced hypoxia-irrelevant free-radical-based cancer therapy. *Small*. 2019;15(51):e1904870. doi:10.1002/smll.201904870
10. Zhu Y, Shi H, Li T, et al. A dual functional nanoreactor for synergistic starvation and photodynamic therapy. *ACS Appl Mater Interfaces*. 2020;12(16):18309–18318. doi:10.1021/acsami.0c01039
11. Huang C, Ding S, Jiang W, Wang FB. Glutathione-depleting nanoplatelets for enhanced sonodynamic cancer therapy. *Nanoscale*. 2021;13(8):4512–4518.
12. Gong L, Zhang Y, Liu C, Zhang M, Han S. Application of radiosensitizers in cancer radiotherapy. *Int J Nanomedicine*. 2021;16:1083–1102. doi:10.2147/IJN.S290438
13. Lu X, Gao S, Lin H, Shi J. Single-atom catalysts for nanocatalytic tumor therapy. *Small*. 2021;17(16):e2004467. doi:10.1002/smll.202004467
14. Zhu Y, Wang W, Cheng J, et al. Stimuli-responsive manganese single-atom nanozyme for tumor therapy via integrated cascade reactions. *Angew Chem*. 2021;60(17):9480–9488. doi:10.1002/anie.202017152
15. Ren SZ, Wang B, Zhu XH, et al. Oxygen self-sufficient core-shell metal-organic framework-based smart nanoplatform for enhanced synergistic chemotherapy and photodynamic therapy. *ACS Appl Mater Interfaces*. 2020;12(22):24662–24674. doi:10.1021/acsami.0c08534
16. Lv B, Zhang H, Zheng X, et al. Structure-oriented catalytic radiosensitization for cancer radiotherapy. *Nano Today*. 2020;35:100988.
17. Jia TT, Yang G, Mo SJ, et al. Atomically precise gold-levonorgestrel nanocluster as a radiosensitizer for enhanced cancer therapy. *ACS Nano*. 2019;13(7):8320–8328. doi:10.1021/acsnano.9b03767
18. Yang Y, Chen M, Wang B, et al. NIR-II driven plasmon-enhanced catalysis for a timely supply of oxygen to overcome hypoxia-induced radiotherapy tolerance. *Angew Chem Int Ed*. 2019;58(42):15069–15075. doi:10.1002/anie.201906758
19. Zhou R, Wang H, Yang Y, et al. Tumor microenvironment-manipulated radiocatalytic sensitizer based on bismuth heteropolytungstate for radiotherapy enhancement. *Biomaterials*. 2019;189:11–22. doi:10.1016/j.biomaterials.2018.10.016
20. Zhu D, Lyu M, Jiang W, Suo M, Huang Q, Li K. A biomimetic nanozyme/camptothecin hybrid system for synergistically enhanced radiotherapy. *J Mater Chem B*. 2020;8(24):5312–5319. doi:10.1039/D0TB00676A
21. Reda M, Bagley AF, Zaidan HY, Yantasee W. Augmenting the therapeutic window of radiotherapy: a perspective on molecularly targeted therapies and nanomaterials. *Radiother Oncol*. 2020;150:225–235. doi:10.1016/j.radonc.2020.06.041
22. Zhang C, Chen W-H, Liu L-H, Qiu W-X, Yu W-Y, Zhang X-Z. An O2 self-supplementing and reactive-oxygen-species-circulating amplified nanoplatform via H2O/H2O2 splitting for tumor imaging and photodynamic therapy. *Adv Funct Mater*. 2017;27(43):1700626. doi:10.1002/adfm.201700626
23. Chen Z, Niu M, Chen G, et al. Oxygen production of modified core-shell CuO@ZrO2 nanocomposites by microwave radiation to alleviate cancer hypoxia for enhanced chemo-microwave thermal therapy. *ACS Nano*. 2018;12(12):12721–12732. doi:10.1021/acsnano.8b07749
24. Bilici K, Atac N, Muti A, et al. Broad spectrum antibacterial photodynamic and photothermal therapy achieved with indocyanine green loaded SPIONs under near infrared irradiation. *Biomater Sci*. 2020;8(16):4616–4625. doi:10.1039/D0BM00821D
25. Gao S, Li T, Guo Y, Sun C, Xianyu B, Xu H. Selenium-containing nanoparticles combine the NK cells mediated immunotherapy with radiotherapy and chemotherapy. *Adv Mater*. 2020;32(12):e1907568. doi:10.1002/adma.201907568
26. Lin L-S, Song J, Song L, et al. Simultaneous fenton-like ion delivery and glutathione depletion by MnO2-based nanoagent to enhance chemodynamic therapy. *Angew Chem Int Ed*. 2018;57(18):4902–4906. doi:10.1002/anie.201712027
27. Luo K, Guo W, Yu Y, et al. Reduction-sensitive platinum (IV)-prodrug nano-sensitizer with an ultra-high drug loading for efficient chemo-radiotherapy of Pt-resistant cervical cancer in vivo. *J Control Release*. 2020;326:25–37. doi:10.1016/j.jconrel.2020.06.005
28. Wang X, Zhong X, Liu Z, Cheng L. Recent progress of chemodynamic therapy-induced combination cancer therapy. *Nano Today*. 2020;35:100946. doi:10.1016/j.nantod.2020.100946

29. Guo D, Huang Y, Jin X, Zhang C, Zhu X. A redox-responsive, in-situ polymerized polyplatinum(IV)-coated gold nanorod as an amplifier of tumor accumulation for enhanced thermo-chemotherapy. *Biomaterials*. 2021;266:120400. doi:10.1016/j.biomaterials.2020.120400
30. Wang S, Yu G, Yang W, et al. Photodynamic-chemodynamic cascade reactions for efficient drug delivery and enhanced combination therapy. *Adv Sci*. 2021;8(10):2002927.
31. Kohli M, MacLean E, Pai M, Schumacher SG, Denkinger CM. Diagnostic accuracy of centralised assays for TB detection and detection of resistance to rifampicin and isoniazid: a systematic review and meta-analysis. *Eur Respir J*. 2021;57(2):2000747. doi:10.1183/13993003.00747-2020
32. Cheng Y, Yang F, Zhang K, et al. Non-fenton-type hydroxyl radical generation and photothermal effect by mitochondria-targeted WSSe/MnO2 nanocomposite loaded with isoniazid for synergistic anticancer treatment. *Adv Funct Mater*. 2019;29(45):1903850. doi:10.1002/adfm.201903850
33. Jibin K, Victor M, Saranya G, et al. Nanohybrids of magnetically intercalated optical metamaterials for magnetic resonance/Raman imaging and in situ chemodynamic/photothermal therapy. *ACS Appl Bio Mater*. 2021;4(7):5742–5752. doi:10.1021/acsabm.1c00510
34. Lyu M, Zhu D, Kong X, et al. Glutathione-depleting nanoenzyme and glucose oxidase combination for hypoxia modulation and radiotherapy enhancement. *Adv Healthc Mater*. 2020;9(11):e1901819. doi:10.1002/adhm.201901819
35. Xia D, Hang D, Li Y, et al. Au-hemoglobin loaded platelet alleviating tumor hypoxia and enhancing the radiotherapy effect with low-dose X-ray. *ACS Nano*. 2020;14(11):15654–15668. doi:10.1021/acsnano.0c06541
36. Zhang G, Ding L, Renegar R, et al. Hydroxycamptothecin-loaded Fe3O4 nanoparticles induce human lung cancer cell apoptosis through caspase-8 pathway activation and disrupt tight junctions. *Cancer Sci*. 2011;102(6):1216–1222. doi:10.1111/j.1349-7006.2011.01930.x
37. Sujai PT, Shamjith S, Joseph MM, Maiti KK. Elucidating Gold–MnO2 core–shell nanoenvelope for real time SERS-guided photothermal therapy on pancreatic cancer cells. *ACS Appl Bio Mater*. 2021;4(6):4962–4972. doi:10.1021/acsabm.1c00241
38. Zhang Y, Cen J, Jia Z, et al. Hepatotoxicity induced by isoniazid-lipopolysaccharide through endoplasmic reticulum stress, autophagy, and apoptosis pathways in Zebrafish. *Antimicrob Agents Chemother*. 2019;63(5):e01639–18. doi:10.1128/AAC.01639-18